# Spray dried TiO$_2$/WO$_3$ heterostructure for photocatalytic applications with residual activity in the dark

Hayat Khan, Marco G. Rigamonti, Gregory S. Patience, Daria C. Boffito*

*Polytechnique Montréal- Dept. of Chemical Engineering, 2900 Boul. Édouard-Montpetit-2500 Chemin Polytechnique, Montréal QC, H3TIJ4, Canada*

ABSTRACT

Synthesizing titanium dioxide with energy storage ability represents a paradigm-shift for photocatalytic applications. We prepared titania tungstated photocatalysts (TiO$_2$/WO$_3$) by sol–gel and crash precipitation methods followed by spray drying to produce a micro-sized hybrid material. X-ray diffraction confirmed the tetrahedral and monoclinic crystalline structure of TiO$_2$ and WO$_3$ in the hybrid material calcined at 600 °C. Spray drying a suspension of titanium hydroxide alone creates spherical 20 μm TiO$_2$ particles, whereas a suspension of ammonium paratungstate dissolved in hydrochloric acid produces 7 μm median size needle like WO$_3$ particles. According to SEM-EDX images, spray drying both semiconductors together produces a homogeneously distributed mixture of the powders. The TW$_{0.075}$ (titanium dioxide/tungsten oxide having 0.075 molar ratio of tungsten precursor) hybrid powder, with a surface area of 221 m$^2$/g, 2.88 eV band gap energy, and 21.5% of anatase [001] facets (Raman analysis), decreased the electron-hole recombination with 1594 ns of carrier lifetime (PL-TRPL analysis). TW$_{0.075}$ outperforms the rest of the samples in the UV degradation of the model pollutant methylene blue (MB), converting 90% MB in 100 min (30 min dark + 40 min light + 30 min dark), thus demonstrating energy storage ability in the absence of UV irradiation. Hydroxyl radicals (OH·) and superoxide anions (O$_2$·$^-$) are the species mainly involved in the pollutant degradation. We propose the transfer pathways mechanism of the photogenerated charge carriers in the hybrid samples.

## 1. Introduction

Titanium dioxide (TiO$_2$) heterogeneous photocatalysis is an advanced oxidation process that degrades a variety of organic compounds, such as synthetic dyes, phenols and chlorophenols, volatile organic compounds, detergents, solvents, heavy metals and pharmaceutical antibiotics. Sunlight as a possible source of irradiation makes TiO$_2$ photocatalysis an attractive technology to degrade pollutants in air. Although TiO$_2$ possesses enticing properties such as chemical stability, strong oxidizing power, photo-resistance, availability, and low cost [1,2], its photocatalytic activity remains insufficient for large-scale applications. Indeed, TiO$_2$ only works in conjunction with irradiation of limited wavelength: TiO$_2$ band gap ($E_g \approx 3.2$ eV) requires $\lambda_{irr}$ < 385 nm, which rules out 95% of the solar spectrum. Moreover, the low rate of oxygen electron transfer from the bulk to the surface and the high recombination rate of photogenerated electron-hole pairs translate to a low photo-oxidation rate [3,4]. Therefore, several strategies such as surface modification of TiO$_2$ with noble metals [5], metal and non-metal doping, composite semiconductors, dye sensitization and ion implantation have been implemented to improve and address the

aforesaid issues [6,7]. Another technique consists of coupling TiO$_2$ photocatalyst with other semiconductors such as ZrO$_2$, CeO$_2$, NiO, Al$_2$O$_3$, Nb$_2$O$_5$, CdS, SnO$_2$, SiO$_2$, V$_2$O$_5$ etc. [8,9]. The expected benefit is the increase of photon absorption due to the improved charge separation because of electronic effects. Storing the photogenerated electrons to release in the dark and to take part in redox processes becomes possible. Besides the improved charge carrier separation, the range of different physical and optical properties of the finished material is an additional advantage [10,11].

Likewise, coupling TiO$_2$ with WO$_3$ is exceptionally appealing because of the physico-chemical properties of WO$_3$: its band gap is relatively short (2.6–2.8 eV), thus requiring longer wavelengths for the excitation. Moreover, it is chemically stable, resilient to photocorrosion, and W exists in 2+, 3+, 4+, 5+, and 6+ oxidation states enabling it to store photogenerated electrons [12,13]. In addition to the demanding application in waste water treatment, tungstated titania (TiO$_2$/WO$_3$) catalysts may activate reactions such as; olefin epoxidation and selective reduction of NO$_x$ in exhaust gases, whereby they act as strong acid and redox catalysts [14]. TiO$_2$/WO$_3$ also possesses a high concentration of acidic sites, which makes it an effective partial

---

* Corresponding author.
  *E-mail address:* daria-camilla.boffito@polymtl.ca (D.C. Boffito).

oxidation catalyst to react glycerol to acrolein [15].

Addressing the photocatalytic properties of $TiO_2/WO_3$ composites, Li et al. [10] synthesized $TiO_2/WO_x$ powders via a sol–gel method: the doped photocatalyst exhibited visible light activity for the degradation of methylene blue. The optimal molar loading of $WO_3$ was 3%, which degraded more than 84% methylene blue in 100 min, compared to $TiO_2$, which only degraded 41%. Su et al. [13] prepared a composite material consisting of amorphous $WO_3$ and crystalline $TiO_2$ via a low temperature peptization method. The authors claim the visible activity of the photocatalyst against methylene blue degradation with a high molar loading of W at 24% [13]. Yang et al. [16] describe the synthesis of the coupled semiconductor ($TiO_2/WO_3$) by a sol–gel method without reporting the photocatalytic activity results. Ke et al. [17] prepared $TiO_2/WO_3$ nanocomposites hydrothermally with cetyl-trimethylammonium bromide (CTAB) as a surfactant. The $TiO_2/WO_3$ with a $TiO_2:WO_3$ ratio of 1 degraded 100% of Rhodamine B (RhB) in 50 min, but $TiO_2$ P25 was as active. Do et al. [18] report the degradation of 60% of 1,4 dichlorobenzene in 10 min by adding 3% $WO_3$ on the surface of $TiO_2$. The current literature reports several complex and time consuming synthesis procedures for $TiO_2/WO_x$ catalysts by physical mixing, dry impregnation, multi-step grafting of ammonium tungstate, improved sol–gel synthesis, coprecipitation, flame spray synthesis, micro arc oxidation, ultrasonic nebulization, flame hydrolysis, hydrothermal method and $WO_3$ or $WO_x$ grafted to the surface of $TiO_2$ [10,17,19–21]. Moreover, Alemany et al. [22] claimed the existence of $WO_3$ in the composite material ($TiO_2/WO_3$) calcined at 1073 K with a tungsten weight fraction of 9% but characterization details were lacking. Similarly, Eibl et al. [14] state that $WO_3$ is formed in tungstated titania when the tungsten loading exceeds a mass fraction of 20% and the powders are calcined above 923 K. In summary, the literature has inadequately characterized the $TiO_2/WO_3$ semiconductor catalyst.

The objective of the present work reflects its originality. We fabricate a uniform and homogenized $TiO_2/WO_3$ composite with a facile method via sol–gel ($TiO_2$) and crash precipitation ($WO_3$), followed by spray drying to produce a microporous micro-sized hybrid material with a minimum input of $WO_3$ precursor (0.1 mol max). The hybrid catalysts are not only photocatalytically active, but also have photo-induced charge storage ability in the dark. We propose a mechanism for the charge-carrier transfer in the hybrid samples.

The photocatalytic activity is a complex function of several factors including crystal structure, particle size via surface area, band gap energy, carrier's recombination, production of active species (super oxide anions, hydroxyl radicals), crystallinity, etc. We characterize the samples by XRD, $N_2$ physisorption, FTIR, Raman, XPS, SEM-EDX imaging, photoluminescence, and time resolved photoluminescence (TRPL) via fluorescence.

## 2. Materials and methods

### 2.1. Chemicals

Titanium butoxide (Ti(oBu)$_4$, purum $\geq$ 97.0% gravimetric), formic acid (reagent grade $\geq$ 95%), ammonium paratungstate hydrate (99.99% trace metal basis, gravimetric) were supplied by Sigma Aldrich, Canada. Fischer Scientific supplied hydrochloric acid (certified ACS plus) and Commercial Alcohols (Boucherville, Quebec, Canada) supplied the anhydrous ethyl alcohol. All the chemicals were used as received without any further purification. Laboratory deionized water was used throughout this work.

### 2.2. Catalyst preparation

$TiO_2$ was synthesized by a simple sol–gel method. Titanium butoxide, anhydrous ethyl alcohol, formic acid and water were mixed for one hour at room temperature (molar ratios 60:500:27:1500).

Anhydrous ethyl alcohol dissolved titanium butoxide under stirring, followed by the drop-wise addition of water and formic acid. Instantaneous hydrolysis occurs in the reaction mixture yielding a milky sol of hydrated titanium hydroxide.

We simultaneously synthesized $WO_3$ by a crash precipitation technique. The molar ratio among ammonium paratungstate (($NH_4$)$_{10}$H$_2$(W$_2$O$_7$)$_6$), hydrochloric acid (HCl) and water was 0.005:200:500. Ammonium paratungstate dissolved in HCl under stirring; afterwards the solution was added rapidly to water, resulting in the crash precipitation of a yellow white precipitate of $WO_3$. We removed most of the water from the precipitate and then washed it several times with deionized water (4 × 100 mL). Finally, we added 20 mL of deionized water to the precipitate under constant stirring to obtain the $WO_3$ suspension.

In a second step, we added the $WO_3$ suspension to the stable sol of titanium hydroxide and stirred the hybrid suspension for 3 h before spray drying it. We followed the procedure reported by Saadatkhah et al. [15], as well as the same equipment (Yamato GB-22 dryer) to produce the final $TiO_2/WO_3$ powders. In the final step the dried powders were annealed at a temperature of 600 °C in a muffle furnace for 2 h to produce the crystalline hybrid $TiO_2/WO_3$ material.

We prepared a set of $TiO_2/WO_3$ powders by varying the $WO_3$ precursor molar ratio at 0.025, 0.05, 0.075 and 0.1. The final material was denoted by TW$_x$, where x is the molar ratio of $WO_3$ precursor. In addition, to produce control $TiO_2$ and $WO_3$, we spray-dried the individual suspension and denoted the final material by T and W, respectively.

### 2.3. Characterization techniques

A Phillips X'PERT diffractometer recorded the X-ray diffraction (XRD) patterns with monochromatic high intensity Cu-kα radiation ($\lambda$ = 1.54178 Å), at a scanning rate of 0.08°/s; the scanning range was $2\theta$ = 10–80°, and the operating conditions were 30 kV and 40 mA.

An LA-950 Horiba laser diffractometer measured the particle size distribution (PSD) of the photocatalysts. We report the median diameter $d_{50}$ and the volume moment mean diameter $D[4,3] = \frac{\sum d_i^4 N_i}{\sum d_i^3 N_i}$, where $N_i$ is the number of particles with the corresponding $d_i$ diameter.

A Quantachrome Autosorb-1 Instrument assisted the textural properties of the photocatalysts by measuring the $N_2$ adsorption and desorption isotherms at 77 K, after degassing the sample under vacuum at 200 °C for 20 h. The specific surface area was calculated with the Brunauer-Emmett-Teller (BET) method ($P/P_0$: 0.05–0.30, C constant: 50–200). The Barrett-Joyner-Hallender (BJH) theory was used to measure the mesopore size distribution (desorption branch, $P/P_0$: 0.15–0.995). The characteristic pore size, volume and specific surface area for the microporous samples (DeBoer thickness) were calculated following the V-t method. We evaluated the total pore volume at the maximum filling pressure ($P/P_0$ = 0.995), integrating for pores smaller than 330 nm in diameter.

Field emission scanning electron microscope (FESEM-JEOL JSM-7600F) equipped with an energy dispersive X-ray (EDX) detector generated images of the powders at several magnification and elemental distribution maps. The microscope operated at a voltage of 10 kV with an energy range of 10 keV.

A TA-Q50 instrument performed thermogravimetric analyses (TGA/DTGA) on a 10 mg sample for 5.0 h. The temperature range varied from 20 to 850 °C with an increase of 3 °C min$^{-1}$. First the sample was heated under nitrogen atmosphere at a flow rate of 20 mL min$^{-1}$ up to a temperature of 120 °C. Afterwards oxygen replaced nitrogen at the same flow rate up to 850 °C.

A Thermo Scientific UV–vis Evolution 300 spectrophotometer equipped with an integrated Pike technologies EasiDiff recorded the diffuse reflectance spectra (DRS) in the range of 190–900 nm, in the analysis potassium bromide (KBr) powder was used a reference.

Raman spectra of the powders were recorded by Renishaw InVia

Reflex Raman microscope with an excitation laser wavelength of 514 nm, laser power of 300 mW and exposure time of 10 s at RT.

A Perkin-Elmer LS- 55 fluorescence spectrometer recorded photoluminescence (PL) spectra at an excitation wavelength of 320 nm of a Xe lamp. A 390 nm cut-off filter rejected the scattered Xe light. Time resolved photoluminescence (TRPL) spectra were obtained with a life spec II spectrofluorimeter (Edinburgh instrument). A laser diode of 375 nm wavelength excited the sample and the decay was measured with a time scale of 0.0048 ns/channel.

X-ray photoelectron spectroscopy (VG ESCALAB 3 Mark II) equipped with X-ray source of Al Kα (1486.6 eV) at a base pressure below $10^{-9}$ Torr was used to investigate the oxidation state of the elements. A survey spectrum first identified all the elements present in the powder, followed by a high-resolution spectrum of the identified elements at a pass energy of 20 eV and 0.05 eV steps. A VG Avantage software processed the data. All peaks were calibrated by setting the major C1 s peak to 285.0 eV, attributed to adventitious carbon.

The hydroxyl radicals (OH·) concentration on the surface of the synthesized powders in water under illumination was measured by a terephthalic acid (TA) fluorescence probe technique [23]. A FluroMax-2 spectrofluorometer equipped with a Xe lamp (excitation wavelength, 350 nm) measured the PL spectra of the produced 2-hydroxyterephthalic acid (TAOH).

### 2.4. Photocatalytic activity

We measured the room temperature photocatalytic activity of the samples in the photodegradation of the synthetic textile dye methylene blue (MB) as a model pollutant. Photocatalyst ($0.2 \, \text{g L}^{-1}$) and MB ($6.0 \, \text{mg L}^{-1}$) were suspended in RO (reverse osmosis) water in separate flasks and sonicated for 20 min to reduce particle agglomeration. We added both the photocatalyst suspension and MB solution to a batch reactor and made up the final volume to 1.5 L with RO water. Before light irradiation the reactor suspension was stirred for 30 min to establish the adsorption/desorption equilibrium. A single UV light source (Germicidal UVC lamp, Atlantic Ultraviolet Corp. GPH212T5L/4, max. output at 254 nm) protected in a quartz sleeve was placed vertically at the center point inside the reactor. Filtered air bubbled continuously throughout the experiment. Each experiment under UV irradiation lasted 40 min. We withdrew 3 mL samples at regular intervals of 10 min. Before the analysis, we filtered the samples (Millipore filters, porosity 0.22 μm) to remove possible catalyst particles. A UV–vis spectrophotometer followed the photocatalytic degradation of MB by measuring at 664 nm the maximum absorbance of MB solution. A Fisher AccumetTMAB15 pH meter equipped with a glass pH electrode measured the *pH* throughout the experiments: the *pH* was constant at 5.6–5.7 in all the activity experiments.

## 3. Results and discussion

### 3.1. X-ray diffraction and particle size distribution analyses

The peak reflections of the XRD patterns of all the catalysts, including control (T, W) and hybrid (TW$_x$) are sharp and intense (Fig. 1a–c). This indicates that the powders are crystalline. Control TiO$_2$ phase (T, Fig. 1a) is pure anatase with a tetragonal structure (ICDD ref. card no. 21-1272). Control WO$_3$ (W, Fig. 1b) exhibits main peaks indexed as monoclinic crystalline structure (ICDD ref. card no. 43-1035). All the main peaks of TiO$_2$ and WO$_3$ have variable intensities depending on their respective amounts in the hybrid samples (TW$_x$, Fig. 1c). This result showed the uniform distribution of both the semiconductors in the hybrid samples. In addition, no phase transformation of TiO$_2$ or of WO$_3$ occurred during the preparation of the hybrid powders: in all the samples TiO$_2$ maintained the anatase structure, while WO$_3$ kept the monoclinic form. In the T sample the diffraction peak of [1 0 1] at 2θ = 25.3° and the peak of [2 0 0] of W at 2θ = 24.3° are the most

intense, indicating that [1 0 1] and [2 0 0] are the major growth directions. We referred to the broadening of these representative peaks to calculate the crystallite size by the Scherrer approximation, defined as: $D = 0.9\lambda/\beta \text{Cos}\theta$, where λ is the X-ray wavelength (15.418 nm), β is the full width at half maximum (FWHM, radians) and θ is the Bragg's angle in degrees. The profile fitting of the recorded XRD spectra using the XRD pattern processing software provided the *FWHM* (full length at half maximum) value of all the peaks. Logically, the crystallite size of TiO$_2$ decreases and that of WO$_3$ increases in the hybrid samples with the increase in WO$_3$ (Table 1): an increase in the tungsten precursor concentration results in a larger crystallite size of hydrated WO$_3$ due to oversaturation and coagulation phenomena [23]. As a consequence, the crystallite size of TiO$_2$ decreases due to the suppressed growth of titania particles in the mixed semiconductors suspension. As evident from the XRD patterns (Fig. 1c) the main anatase peaks [101], [004], [200], [105] and [204] at 2θ = 23.5°, 37.4°, 48.1°, 53.9° and 62.7° broaden along with the decrease in peak intensity with increase in WO$_3$.

We report the particle size distribution (PSD) in water of the calcined powders in Fig. 1d, and the volume moment mean diameter *D* [4,3] and the median diameter $d_{50}$ in Table 1. Control W has the lower *D*[4,3] and $d_{50}$ at 6.3 and 6.0 μm, while control T has *D*[4,3] and $d_{50}$ at 13.3 and 11.1 μm, respectively, indicating that WO$_3$ particles are less susceptible to coagulate in solution. This is an advantage to the photocatalytic activity, which decreases with a decrease in the active surface area and reduced access of the light to the catalyst inner surface as a consequence of particle agglomeration. The particle size distribution of the hybrid powders further support this observation: the *D*[4,3] and $d_{50}$ diameters decrease with an increase in WO$_3$ content.

### 3.2. BET surface area and pore size distribution analyses

The BET and BJH analyses provided the textural properties, i.e. the surface area, pore volume and size of the photocatalytic powders (Table 2). We report the N$_2$ adsorption-desorption isotherms of the calcined powders in Fig. S1 (supplementary information). Instrument accuracy were ± 2 m$^2$/g, ± 0.01 m$^3$/g and ± 0.1 nm for specific surface area, pore volume and pore diameter, respectively. According to the IUPAC classification [24], all samples exhibit an overlapping type 1(b) – type 2 isotherm, indicating the coexistence of micro, meso and macropores. Type 1(b) is typical of materials having narrow mesopores (< 2.5 nm) and a broad micropore size distribution, while type 2 reveals a macroporous structure due to the lack of plateau at the maximum filling pressure. Moreover, all samples have a type H3 hysteresis, associated to plate-like aggregates connected through a network of macropores, incompletely filled with the adsorbate. The BET results (Table 2) indicate that the hybrid materials have higher surface area than control T and W powders, except TW$_{0.1}$. This may be due to the different crystal structure with respect to titanium dioxide and tungsten oxide, which may have a role in decreasing the agglomeration among particles. In addition, in the hybrid samples the surface area decreases with increasing tungsten precursor concentration beyond 0.075 mol. Moreover, the pore size distribution is in the 1.4–3.4 nm range (V-t method) for TW$_x$ powders, compared to 3.4 and 1.7 nm for the control T and W, respectively. Therefore, in the case of TW$_{0.075}$ (titanium dioxide/tungsten oxide having 0.075 molar ratio of tungsten precursor) and TW$_{0.01}$ a mechanically strong particle network may form due to a better packing of TiO$_2$ and WO$_3$ primary particles. Further increasing WO$_3$ prevents nanoparticles from structuring in a homogeneous matrix during the spray drying and results in larger pores than control W and hybrid TW$_{0.025}$, TW$_{0.05}$ samples. A high surface area and the presence of micro and mesopores (Table 2) are expected to impact positively the photocatalytic performance. A high $S_{BET}$ translates into a high concentration of active sites, and a porous structure facilitates the adsorption of the molecules to degrade [25].
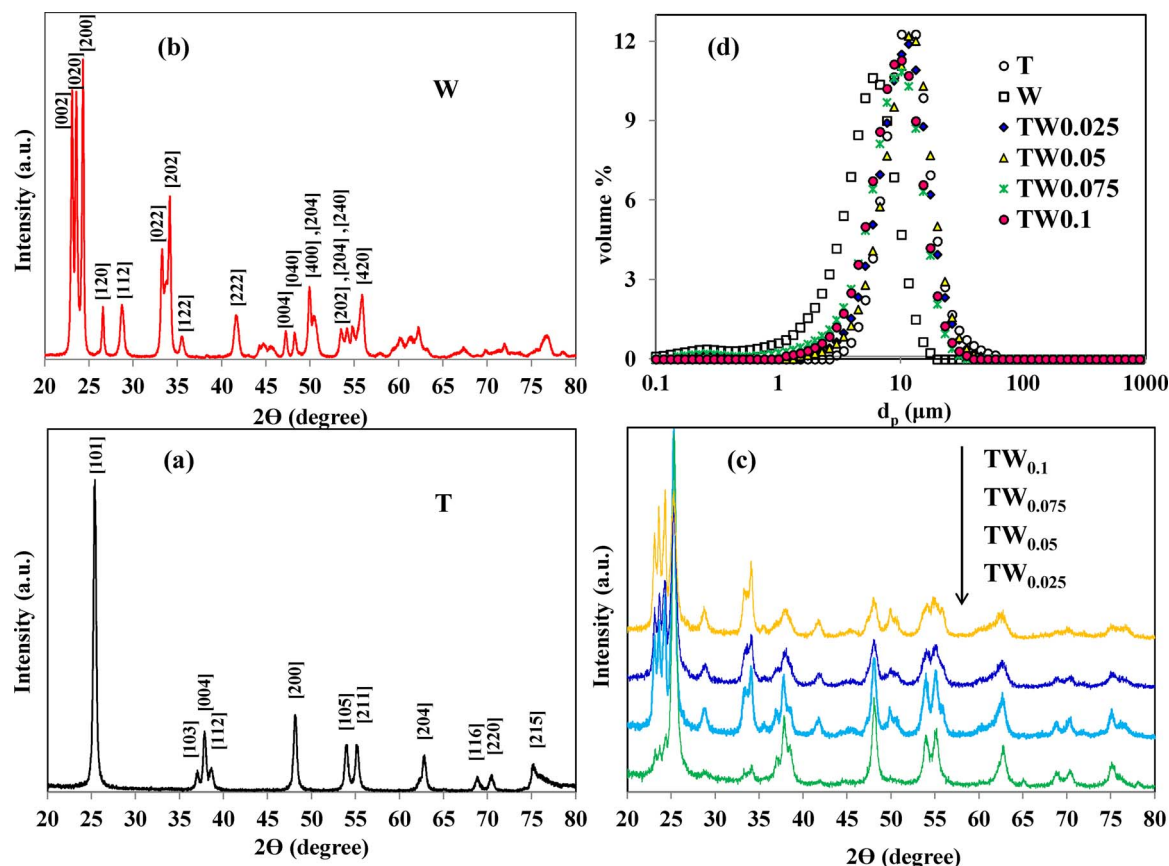
Fig. 1. (a–c) XRD diffraction patterns and (d) PSD distribution of the samples calcined at 600 °C.

**Table 1**
Crystallite size, mean and median particles distribution and band gap energy values of the prepared samples calcined at 600 °C.

| Sample | Crystallite size[a] (nm) | | Mean, D [4,3][b] (µm) | Median $d_{50}$ (µm) | Band gap (eV) | | |
|--------|---------|---------|---------|---------|---------|---------|---------|
| | | | | | $E_g$ | $E_{g1}$ | $E_{g2}$ |
| T | 23.0 | | 13.0 | 11.0 | 3.19 | | |
| W | | 24.0 | 6.0 | 6.0 | 2.62 | | |
| $TW_{0.025}$ | 18.0 | 24.0 | 14.0 | 13.0 | 3.13 | 3.13 | 3.02 |
| $TW_{0.05}$ | 16.0 | 25.0 | 12.0 | 11.0 | 3.06 | 3.06 | 2.72 |
| $TW_{0.075}$ | 15.0 | 26.0 | 12.0 | 11.0 | 2.89 | 2.93 | 2.63 |
| $TW_{0.1}$ | 12.0 | 21.0 | 11.0 | 10.0 | 2.86 | 2.92 | 2.60 |

[a] The uncertainty in crystallite size is < 1.0 nm.
[b] The uncertainty in mean D[4,3] is < 2.0 nm.

**Table 2**
Textural properties of the calcined samples by $N_2$ physisorption.

| Sample | BET surface area ($m^2$/g) | Total pore volume ($cm^3$/g) | Pore diameter (nm) |
|--------|---------|---------|---------|
| T | 34.0 | 0.06 | 3.4 |
| W | 99.0 | 0.24 | 1.7 |
| $TW_{0.025}$ | 166.0 | 0.32 | 1.4 |
| $TW_{0.05}$ | 180.0 | 0.39 | 1.7 |
| $TW_{0.075}$ | 221.0 | 0.35 | 3.4 |
| $TW_{0.1}$ | 149.0 | 0.55 | 3.0 |

### 3.3. Electron microscopy analysis

We report the field emission scanning electron microscope (FESEM) micrographs of control T and W and hybrid ($TW_{0.075}$) powders calcined at 600 °C Fig. 2. Control T sample particles are spherical, have a uniform particle diameter of 100 nm, and their surface is smooth (Fig. 2a). In the control W powder, the big spheres bulks (around 10 µm) are agglomerates of smaller particles having needle like morphology. Moreover, intra-particle porous structure in the $WO_3$ bulk is evident (Fig. 2b insert), differently from control $TiO_2$ (Fig. 2a insert). In the hybrid $TW_{0.075}$ powder (Fig. 2c), surprisingly, although the spherical morphology of $TiO_2$ particles is maintained, there are no bulky spherical particles of $WO_3$, as if there was no $WO_3$ agglomeration: the needle-like structure of $WO_3$ persists. $WO_3$ tends to crystallize in needle like structures, regardless of the synthetic method, being this crash precipitation method, spray drying [15], chemical vapor deposition (CVD) [26], in which the authors performed plasma bombardment of W followed by oxidation, hydrothermal method [27] combustion synthesis [28] and low temperature solvothermal synthesis [29]. The XRD analysis of crystallite size, as well as the increased BET surface area of the composite samples confirmed that $WO_3$ did not agglomerate in the hybrid samples with a $WO_3$ precursor content up to 0.075 mol.

In traditional composite synthetic methods such as sol–gel, precipitation and hydrothermal method the components are mixed by magnetic stirring or by sonication, and then dried in an oven, furnace or Teflon reactor. The result is usually non-uniform particle agglomeration. With the method presented here the distribution homogeneity between the two different semiconductors ($TiO_2$ and $WO_3$) is excellent. The nozzle of the spray-dryer atomized fine droplets of the sample precursor dry instantaneously by a stream of hot air (100 °C). The SEM-EDX analysis confirms the homogeneity of the samples (Fig. 2d, $TW_{0.075}$). The elemental mapping reveals both T and W as evenly distributed throughout the hybrid sample. This translates into a high degree of $TiO_2$-$WO_3$ contact. A high interparticle connection network results in higher charge separation and higher charge transfer changes between the two semiconductor oxides [30].
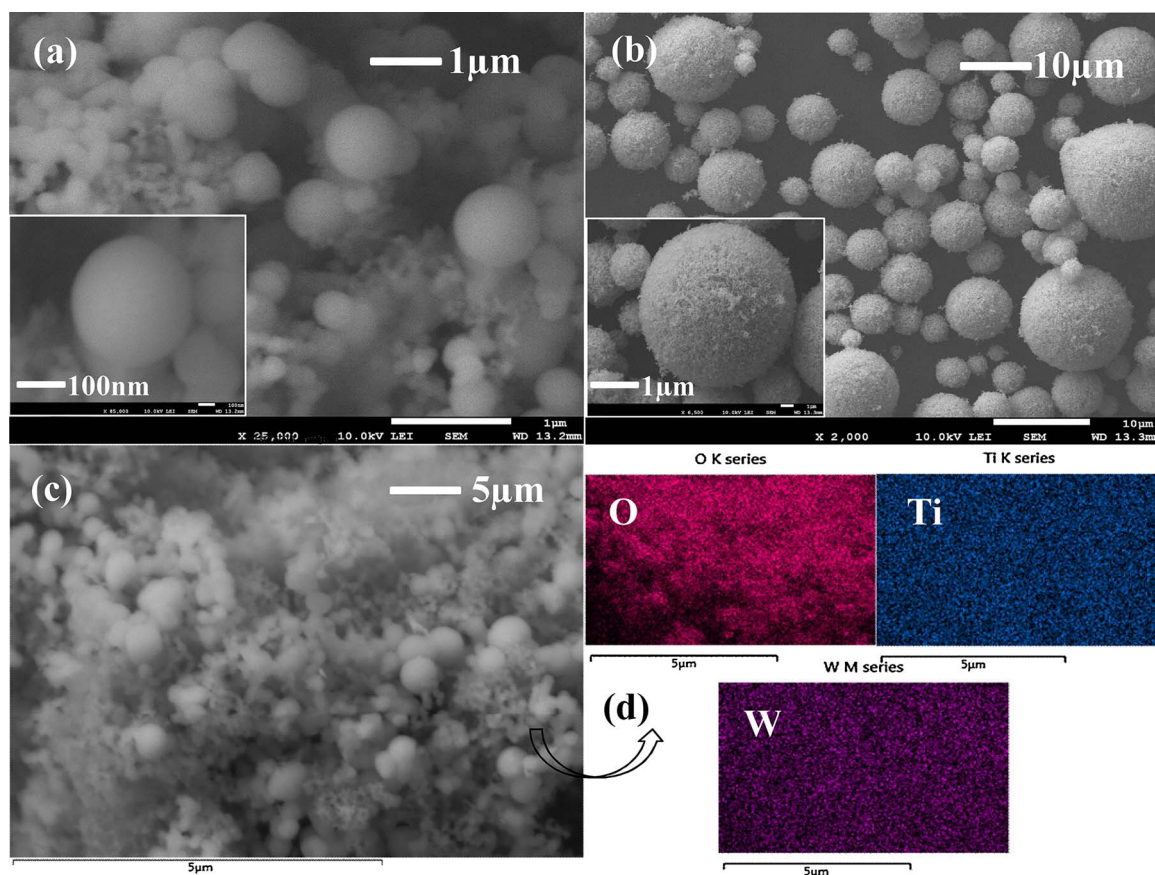
**Fig. 2.** SEM images of the calcined powders; (a) control T (b) control W (c) $TW_{0.075}$ and (d) SEM-EDX elemental mapping of O, Ti and W in $TW_{0.075}$ sample.

### 3.4. TGA/DTGA analysis

We performed the thermogravimetric (TGA) and differential thermal analysis (DTGA) of the control samples (T and W) and of hybrid samples ($TW_{0.025}$ and $TW_{0.075}$) to explore the weight change of the material a function of temperature from 25 °C to 850 °C at a ramp of 3 °C/min. T, W, $TW_{0.025}$, and $TW_{0.075}$ powders showed a total weight loss of 29.1%, 9.4%, 28.1% and 22.5%, respectively (Fig. 3). The evaporation of adsorbed and chemisorbed water, the volatilization and thermal decomposition of the solvent (ethanol) and of reaction co-products (butanol from titanium precursor and ammonia from tungsten precursor) occurs below 120 °C. The carbonization or combustion of organic compounds i.e. loss of carbon, hydrogen and oxygen is responsible for the peaks between 120 and 300 °C. This weight loss results in the endothermic peak at 198 °C in control T, while in control W and hybrid ($TW_x$) samples it is at 185 °C. After this temperature the sample weight is constant. Moreover, as described earlier the weight loss is minimum in control W compared to control T sample. We ascribe it to the tungsten linkages with water such as W-OH, W-O, O-W-O formed during the crash precipitation process [31]. The thermogravimetric behavior of the hybrid samples confirm this observation. In $TW_{0.075}$ the total weight loss decreases compared to $TW_{0.025}$ because the $WO_3$ content increases reducing water evaporation. The FTIR data presented later further support this result. Furthermore, the control W and of the hybrid samples gained weight beyond 650 °C (dotted arrow in Fig. 3), which indicates oxygen gain as a result of $WO_3$ oxidation and crystallization processes.

### 3.5. FTIR analysis

In the FTIR spectrum of control T (Fig. 4a) the broad absorption peak in the range 450–850 $cm^{-1}$ corresponds to Ti−O−Ti vibrational frequencies and Ti−O stretches [11]. Peaks at 1350 and 1527 $cm^{-1}$ belong to the symmetric $\upsilon(COO)_s$ and asymmetric $\upsilon(COO)_{as}$ carboxylate stretches, respectively [32] from the formic acid. The very intense peak at 2345 $cm^{-1}$ is unexpected and corresponds to atmospheric $CO_2$ adsorption, meaning that pure titanium dioxide is prone to atmospheric contamination. The broad absorption peak in the range of 3050–3600 $cm^{-1}$ belongs to Ti−OH stretching modes of molecular water. The strong absorption peak for control W is in the 650–950 $cm^{-1}$ range, which corresponds to the stretching modes of O−W−O bonds [33]. The four peaks at 1435, 1620, 1860 and 2075 $cm^{-1}$ belong to [OH, W−O], bending mode of coordinated water (H−O−H) and O−H, respectively [34]. The bands in the region of 3200–3600 $cm^{-1}$ are ascribed to the W-OH stretching [35]. In the FTIR spectra of hybrid powders (Fig. 4b) there are two distinctive peaks: the characteristic bending mode of coordinated water at 1635 $cm^{-1}$, and the deep trough in the region 3100–3600 $cm^{-1}$ centered at 3450 $cm^{-1}$ due to OH groups. The intensity of both these peaks increases with an increase in $WO_3$. The peaks also become narrower compared to the control samples, indicating that a high degree of hydroxyl groups binds onto the surface of the hybrid powders. These hydroxyl groups play a significant role in the photocatalytic process, as they act as scavengers for the photogenerated holes to produce the powerful hydroxyl radicals (OH·) oxidants, which decompose organic compounds.

### 3.6. Diffuse reflectance analysis

Diffuse reflectance spectroscopy (DRS) quantified the optical properties of the control and hybrid materials. We measured the band gap energies with the equation; $\alpha h\vartheta = C (h\vartheta - E_g)^n$, where $\alpha$, $h$, $v$, $E_g$ and $A$ are the absorption coefficient, the Plank constant, light frequency, band gap and a constant. The UV–vis absorption spectra yielded the reflectance ($R$) spectra ($R = 10^{-A}$; $A$ is optical absorbance). The
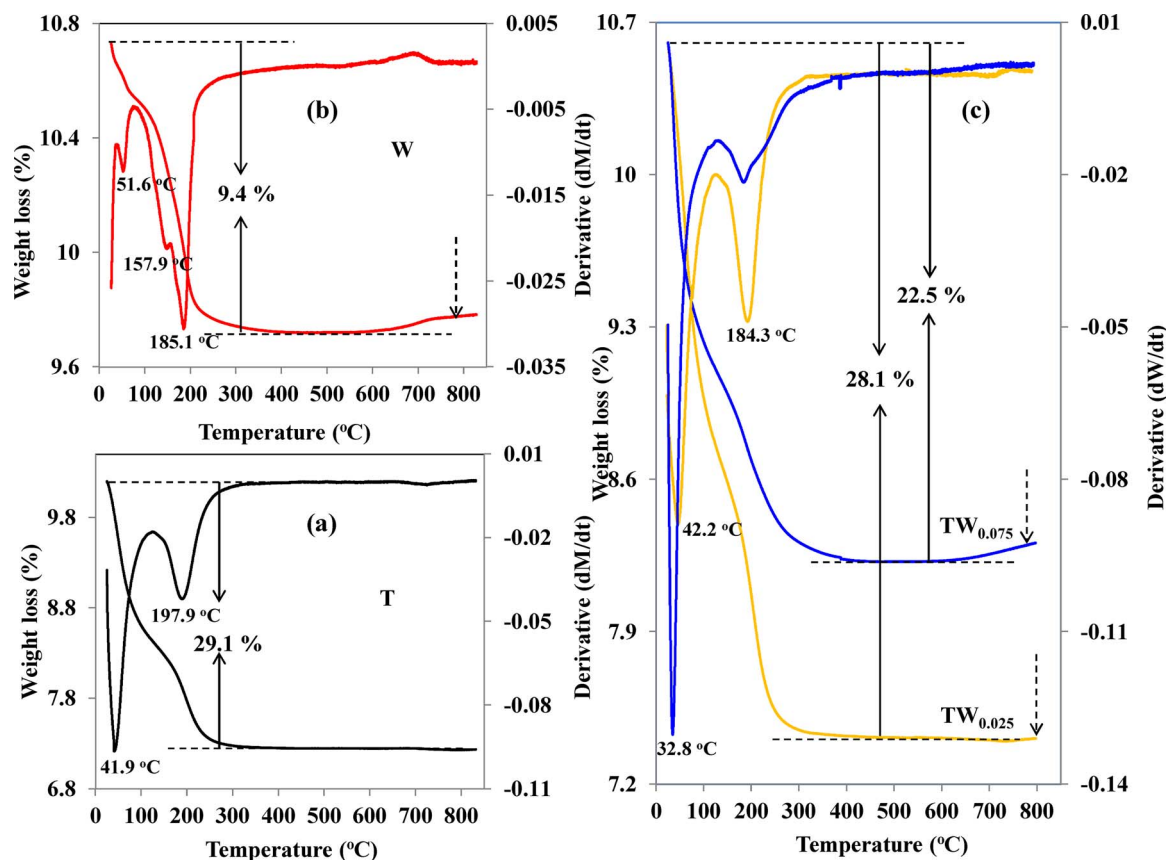
**Fig. 3.** TGA/DTGA curves of (a) control T and (b) W and of hybrid samples (c) $TW_{0.025}$ and $TW_{0.075}$.

Kubelka–Munk formalism [25] converted the optical reflectance into the equivalent absorption coefficient ($\alpha$) proportional to Kubelka–Munk function $F(R)$: $F(R) = \alpha = \frac{(1-R)^2}{2R}$. In the Tauc plot $(\alpha h\vartheta)^n$ versus $h\vartheta$, the band-gap ($E_g$) value is measured from the intersection point of the two tangents lines, one drawn on the straight part of the y-axis $((\alpha h\vartheta)^n)$ while the second one is drawn parallel (x-axis) on the tail section of the curve. The value of the exponent $n$ is ½ for both $TiO_2$ and $WO_3$ because they both have indirect band transitions. Fig. 5 reports the Tauc plot of the samples. The band gap energy for the control T and W samples was 3.19 eV (389.7 nm) and 2.62 eV (474.5 nm), respectively (Table 3), meaning that the absorption onset for control $TiO_2$ (T) is in the UV region, compared to the visible light absorption onset for control $WO_3$ (W). Increasing the $WO_3$ content a red shift was observed towards longer wavelength compared to control T sample: W > $TW_{0.01}$ > $TW_{0.075}$ > $TW_{0.05}$ > $TW_{0.025}$ > T. This indicates that all the $TW_x$ powders absorb in the region of 398–480 nm, suggesting the hybrid powders may be active in the visible light range. The visible light activity of the samples is beyond the scope of the present work. In summary, the decrease in the band gap energy leads to rapid photo-excitation of electrons from the lower lying valance band (VB) to the conduction band (CB), which increase the photocatalytic activity, as well as electron storage to be exploited later in the absence of light irradiation.

$TW_{0.05}$ and $TW_{0.1}$ (Fig. 5 inserts) exhibit two steep optical absorption thresholds. In $TW_{0.05}$ sample, the first one is from 351 to 381 nm and the second one is from 381 to 427 nm. The first absorption edge corresponds to the band gap of $TiO_2$, which results in the photo-excitation of electrons from the $TiO_2$ VB band to the $TiO_2$ CB band under UV light, while the second absorption edge corresponds to the band gap of $WO_3$. This causes the photo-excitation of electrons from the $WO_3$ VB band to the $WO_3$ CB band under both UV and visible light irradiation.

To investigate the band potential of the samples, we calculated the valance band (VB) and conduction (CB) potential by the following equations [36,37]: $E_{VB} = X - E^e + 0.5E_g$; $E_{CB} = E_{VB} - E_g$. $E_{VB}$ and $E_{CB}$ are the VB and CB edge potential, $X$ is the absolute electronegativity of the semiconductor ($X_{TiO2} = 5.81$ eV and $X_{WO3} = 6.59$ eV). $E^e$ is the energy of the free electrons on the hydrogen scale ($\sim 4.5$ eV) and $E_g$ is the band gap energy. The calculated VB and CB potential of control $TiO_2$ (T) are 2.91 and $-0.29$ eV, and for control $WO_3$ (W) they are 3.4 and 0.78 eV, respectively. The CB potential of $TiO_2$ is more negative than that of $WO_3$: under light irradiation, the photogenerated electrons will transfer from the CB of $TiO_2$ to the one of $WO_3$, and similarly the photogenerated hole will transfer from the VB of $WO_3$ to those of $TiO_2$, because the VB potential of $WO_3$ is more positive than that of $TiO_2$. The hybrid samples follow the same trend in the band potential with softer variations (Table 3). Therefore, mixing $TiO_2$ and $WO_3$ reduces the electron–hole recombination, leading to an increase in the interfacial photoinduced charge separation and consequently to an enhanced photocatalytic activity.

### 3.7. Raman spectroscopy analysis

Peaks at 143.8 cm$^{-1}$ (1-$E_g$), 197.3 cm$^{-1}$ (2-$E_g$), 390.0 cm$^{-1}$ ($B_{1g}$), 515.2 cm$^{-1}$ ($A_{1g}$) and 639.1 cm$^{-1}$ (3-$E_g$) in the Raman spectrum of the control T powder are typical of the anatase tetragonal structure [25] (Fig. 6a). In the control W (Fig. 6b), the peak at 181.3 cm$^{-1}$ is assigned to W−W bond, while the peaks at 137, 274.4 and 327.7 cm$^{-1}$ relate to the bending vibration of W−O−W bond. The peaks at high wave number of 717.7 cm$^{-1}$ correspond to O−W−O vibration, and 807.2 cm$^{-1}$ corresponds to the crystalline $WO_3$ stretching vibration of the bending oxygen of W−O−W. Notably, these peaks are typical vibrational modes of monoclinic $WO_3$ and the Raman peaks at 717 and 807 cm$^{-1}$ are the two fingerprint peaks representing the crystalline monoclinic $WO_3$ [38,39]. All peaks observed for control T and W,
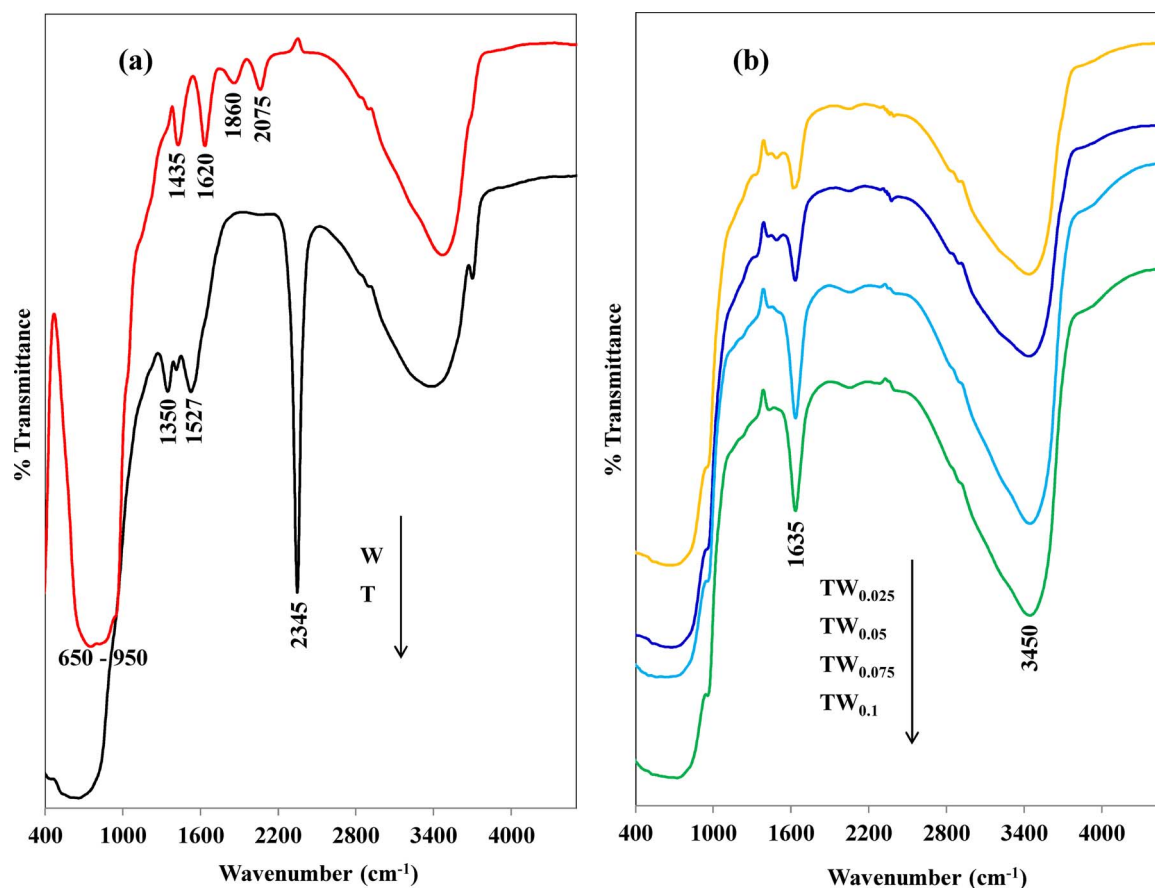
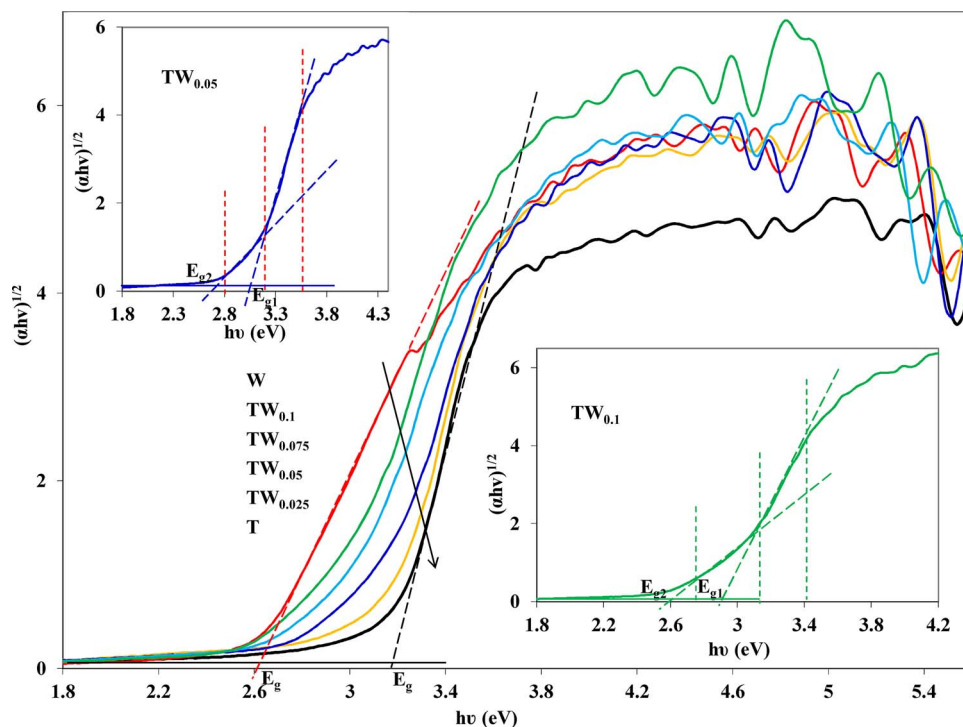**Fig. 4.** FTIR spectra of the control and hybrid powders calcined at 600 °C.



**Fig. 5.** Tauc plots of the prepared powders calcined at 600 °C. Inserts-Tauc plots of $TW_{0.05}$ and $TW_{0.1}$ showing the two semiconductors band position.

appear in the Raman spectrum of the hybrid samples (Fig. 6c). The Raman peaks intensity varies with the $WO_3$ content. Since no other peaks are present, the samples were highly pure. Moreover, we did not observe any Raman peak shift. For instance, the representative intense

Raman peak of anatase (143.8 cm$^{-1}$, 1-$E_g$) in the insert of Fig. 6c, does not shift, indicating the stability of the tetragonal anatase phase. We can derive the same conclusion for the monoclinic $WO_3$ phase.

The [001] planes of $TiO_2$ anatase is the most photocatalytically

**Table 3**
Calculated CB and VB band potentials, measured $TiO_2$ Raman peak intensity and the ratio of Raman vibrational modes between $1$-$E_g$ and $A_{1g}$ for the synthesized calcined powders.

| Sample | Band potential (eV) | | | | Raman peaks intensity | | Percentage of [001] planes |
|---|---|---|---|---|---|---|---|
| | $TiO_2$ | | $WO_3$ | | $1$-$E_g$ (144 cm$^{-1}$) | $A_{1g}$ (515 cm$^{-1}$) | |
| | $E_{VB}$ | $E_{CB}$ | $E_{VB}$ | $E_{CB}$ | | | |
| T | 2.91 | −0.29 | | | 20763.8 | 1298.9 | 6.3 |
| W | | | 3.40 | 0.78 | | | |
| $TW_{0.025}$ | 2.88 | −0.26 | 3.60 | 0.59 | 34317.3 | 3142.5 | 9.2 |
| $TW_{0.05}$ | 2.84 | −0.22 | 3.45 | 0.73 | 16993.4 | 1898.5 | 11.2 |
| $TW_{0.075}$ | 2.78 | −0.16 | 3.41 | 0.78 | 10334.8 | 2218.2 | 21.5 |
| $TW_{0.1}$ | 2.77 | −0.15 | 3.38 | 0.80 | 10104.0 | 1134.1 | 11.2 |

active, because of the enhanced adsorption and electronic properties. Tian et al. [40] report Raman spectroscopy as a method to measure the percentage of the exposed [001] planes from the micro perspective of molecular bonding with the least uncertainty. Following this procedure, the Raman peak intensity ratio of the $E_g$ (143.8 cm$^{-1}$) and $A_{1g}$ (515.2 cm$^{-1}$) in control T and in hybrid ($TW_x$) samples provides the percentage of the exposed [001] planes of $TiO_2$ anatase. The percentage of [001] planes of $TiO_2$ anatase increases up to the maximum 21.5% for the hybrid $TW_{0.075}$ sample, and afterwards it decreases by further increasing the $WO_3$ content. In summary varying the concentration of $WO_3$ up to a value increases the [001] planes of $TiO_2$ anatase, likely resulting in an enhanced photocatalytic activity.

### 3.8. Photoluminescence analysis

Photoluminescence (PL) emission provide information on the electron-hole recombination as the recombination of excitons pairs produces energy in the form of fluorescence. The lower PL intensity, the lower the recombination rate and the higher the activity [34]. We examined the PL spectra of the samples excited at 320 nm in the wavelength range of 380–650 nm (Fig. 7a). Control $WO_3$ (W) is intensely photoluminescent (broad band), having a maximum violet emission that peaks at 468 nm (mainly associated with oxygen and surface related trap states [41]). The peak intensity is much higher than that in the spectra of control $TiO_2$ (T) and hybrid ($TW_x$) samples. The PL intensity greatly decreases after the coupling of the two semiconductors ($TiO_2/WO_3$): W > T > Degussa P25 ≈ $TW_{0.1}$ > $TW_{0.025}$ > $TW_{0.05}$ > $TW_{0.075}$, implying that energy-wasteful charge recombination suppresses as a consequence of the efficient electron-hole transfer between $TiO_2$ and $WO_3$. The PL intensity increases again when the content of $WO_3$ precursor exceeds 0.1 mol as in $TW_{0.1}$. As we report in Section 3.6, the photoexcited electrons transfer from $TiO_2$ to the $WO_3$ conduction band and the holes accumulate in the $TiO_2$ valence band, thus being separated. The PL trend suggests that when the content of $WO_3$ precursor is lower than the optimal amount (0.075 mol), $WO_3$ energy level act as a separation center. On contrary when the amount of $WO_3$ is higher than its optimal amount, $WO_3$ energy
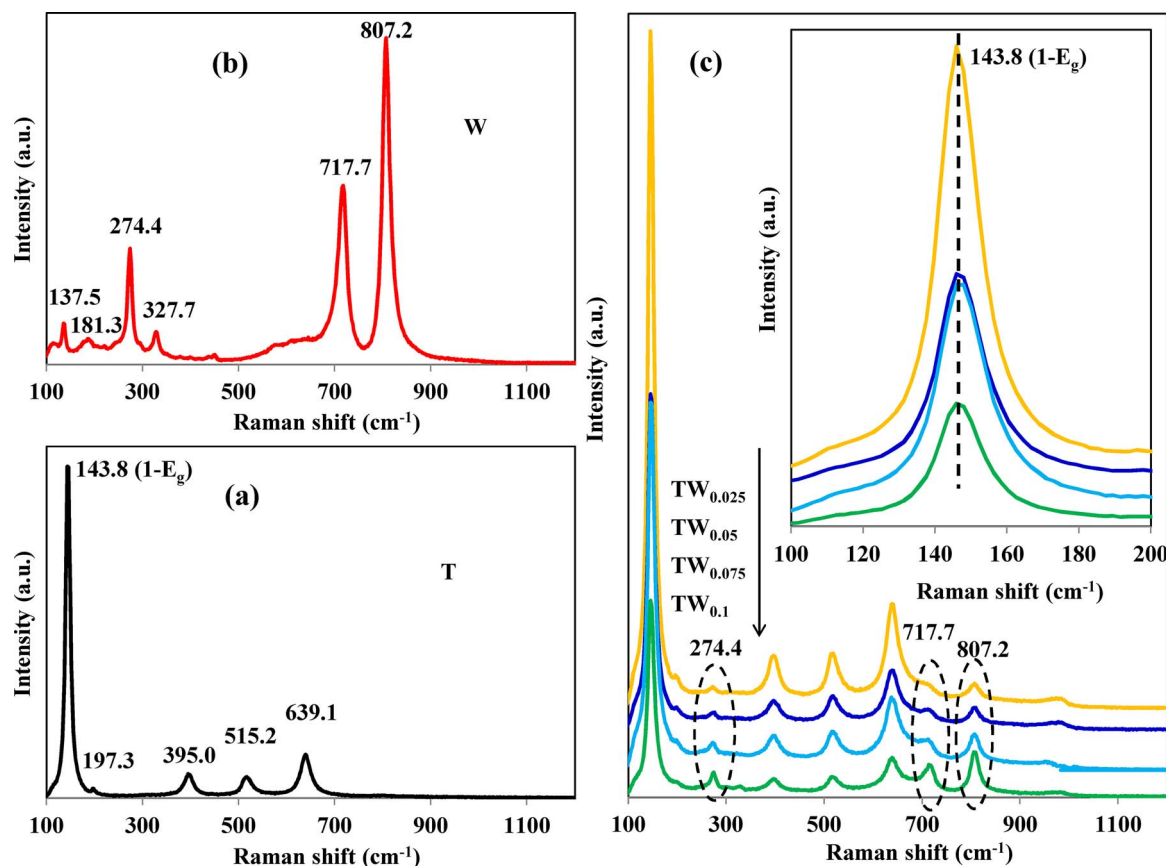
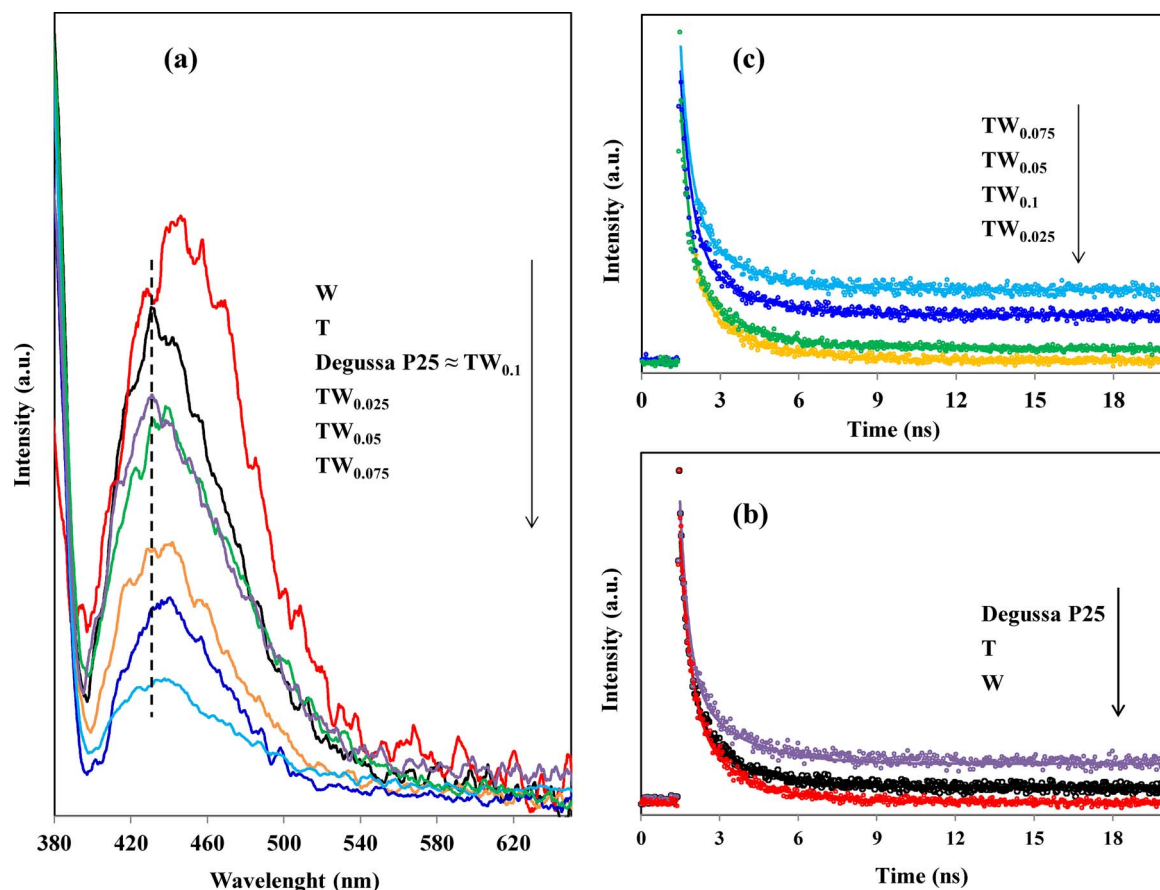**Fig. 6.** Raman spectra of the samples calcined at 600 °C.

**Fig. 7.** (a) Photoluminescence (PL) and (b and c) time resolved photoluminescence (TRPL) of the samples calcined at 600 °C. The TRPL curves are fitted bi-exponentially with a correction, $R^2 = 0.995$.

level act as a recombination center.

The PL spectrum of control T and of commercial Degussa P25 exhibits a violet emission that peaks at 432 nm, possibly resulting from the self-trapped excitons (STE) localized on the $TiO_6$ octahedra [3]. After photo-irradiation at 320 nm, the electrons in the conduction band move through the ionic lattice, interacting with the lattice ions. The localized electrons capture hole and generates self-trapped excitons. This 432 nm violet peak of control T (dotted lines in Fig. 7a) gradually shifts towards higher wavelength with increasing $WO_3$ content. This red shifting of the violet emission peak is due to the synergistic effect of the two semiconductors (band gap renormalization effect). The interaction of the $TiO_2$ conduction band electrons with the $WO_3$ conduction band electrons results in the shrinkage of the combined band gap and the effective shifting of the violet peak emission to lower energy. This shift of the emission peak (432 nm in control T) towards longer wavelength in hybrid powders further supports the decrease of the band gap of $TiO_2$ due to $WO_3$ coupling effect (Table 3).

Therefore, based on PL analysis the hybrid powders should be more active photocatalytically than control powders. The photocatalytic activity is proportional to the transfer rate of the electron-hole pairs to the redox reactions and inversely proportional to the photogenerated excitons recombination rate. The decrease in the crystallite size of the catalyst, which increases the surface area (Table 2) along with the interfacial charge-carrier transfer also decrease the PL intensity.

Time resolved photoluminescence (TRPL) provides information on the lifetime of the charge carriers in the samples. Fig. 7b–c report the TRPL curves of the samples excited at 475 nm. A bi-exponential fitting was the best for the TRPL curves:

$$y = y_o + \alpha_1 \exp\left(\frac{-t}{\tau_1}\right) + \alpha_2 \exp\left(\frac{-t}{\tau_2}\right)$$

Where $y_o$ is the base line correction (y-offset), $\tau_1$ and $\tau_2$ are the excited state emission decay time and $\alpha_1$ and $\alpha_2$ are the pre exponential factors. The following equation calculates the average life time [41].

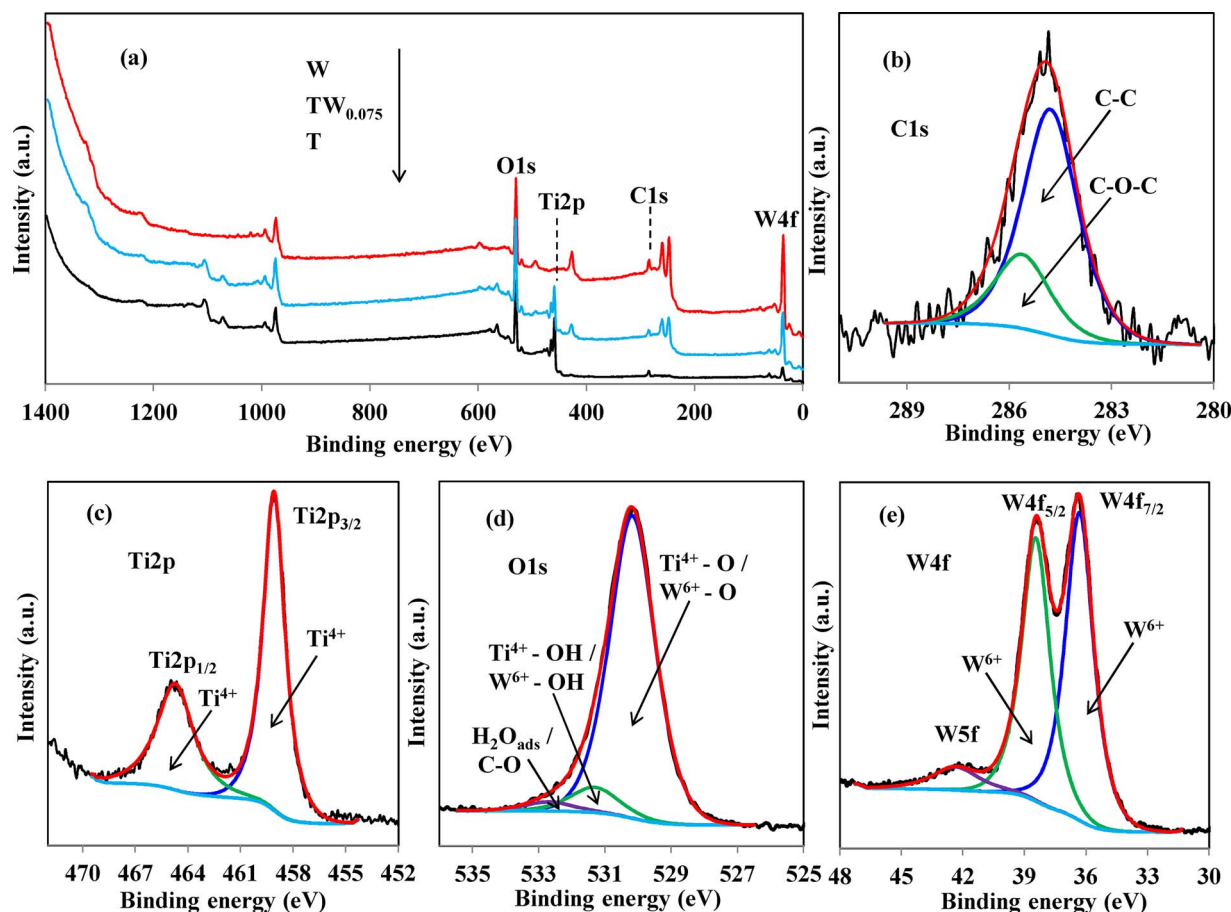$$\tau_{av} = \frac{\alpha_1 \tau_1^2 + \alpha_2 \tau_2^2}{\alpha_1 \tau_1 + \alpha_2 \tau_2}$$

The hybrid samples $TW_{0.05}$ and $TW_{0.075}$ have the longest charge carrier lifetime (Table 4) at 1310 ns and 1594 ns, which support the PL analysis results. Several factors such as structural defects (oxygen vacancies), mobility of the carriers, band structure etc. are responsible for the charge carrier life-time [42]. In our case, the longer lifetime of the charge carriers is due to the indirect band structure and the difference in the bands potentials of the two semiconductors. Since $TiO_2$ and $WO_3$ have indirect band structure, the conduction band (CB) electrons and valence band (VB) holes will be in different positions in the Brillouin zones. Also, as a consequence of the difference in band potentials, the $TiO_2$ CB electrons will diffuse to the CB of $WO_3$ rather than directly to the $TiO_2$ VB band to recombine with holes. As an analogy, for commercial Degussa P25 the longer lifetime of photogenerated carriers compared to control T and W is attributed to its hybrid nature, i.e. the presence of both anatase and rutile phases.

### 3.9. X-ray photoelectron spectroscopy analysis

X-ray photoelectron spectroscopy (XPS) determined the chemical composition in atomic percentages of the elements (Table 4) and the valance states in the control T and W samples, and in the hybrid powders. We further analyzed the XPS spectrum of the hybrid powders by high resolution deconvolution of the C (1s), Ti (2p), O (1s) and of W (4f). We only report the XPS spectrum of $TW_{0.075}$ as a representative of

**Table 4**
Average life time period ($\tau_{av}$, ns) of the charge carriers and XPS elemental composition (at.%) of the calcined powders.

| Sample | TRPL parameters values | | | | | Atomic percent (at.%) | | | |
|---|---|---|---|---|---|---|---|---|---|
| | $\alpha_1$ | $\tau_1$ (ns) | $\alpha_2$ | $\tau_2$ (ns) | $\tau_{av}$ (ns) | C1s | T2p | O1s | W4f |
| Degussa P25 | 920.5 | 424.2 | 214.1 | 1416.5 | 858.0 | | | | |
| T | 900.7 | 459.9 | 209.7 | 1150.3 | 714.0 | 13.7 | 22.7 | 66.3 | |
| W | 912.7 | 403.9 | 202.9 | 1250.0 | 749.0 | 20.0 | | 62.8 | 17.1 |
| TW$_{0.025}$ | 756.2 | 430.4 | 200.9 | 1700.0 | 1080.0 | 10.6 | 17.9 | 65.8 | 5.6 |
| TW$_{0.05}$ | 809.0 | 360.7 | 258.9 | 1879.4 | 1310.0 | 8.4 | 15.2 | 67.5 | 8.9 |
| TW$_{0.075}$ | 513.4 | 459.4 | 209.7 | 2179.42 | 1594.0 | 10.7 | 14.2 | 65.0 | 10.1 |
| TW$_{0.1}$ | 809.0 | 360.7 | 258.9 | 1609.4 | 1095.0 | 7.9 | 13.9 | 65.7 | 12.5 |



**Fig. 8.** XPS spectra of the calcined (a) control T, W and hybrid TW$_{0.075}$ powders, high resolution spectra of (b) C1s, (c) Ti2p, (d) O1s, and (e) W4f of the TW$_{0.075}$ powder.

the hybrid samples for the sake of brevity (Fig. 8). Ti, W, and common oxygen and carbon peaks are all present in the TW$_{0.075}$ sample (Fig. 8a). The calibration of all peaks referred to the C1 s species, corresponding to the adventitious carbon from the XPS instrument. Deconvoluting the peaks of C1 s (Fig. 8b) yields two peaks representing two carbon bonding configurations: the binding energy at 284.8 eV and 285.6 eV corresponds to C−C and C−O−C, respectively. The latter is ascribable to atmospheric contamination. The Ti2p spectrum (Fig. 8b) exhibits the two characteristic doublets for Ti2p$_{3/2}$ at binding energies of 456.0 eV and 459.1 eV and for Ti2p$_{1/2}$ at bonding energies of 463.0 eV and 464.3 eV. The peaks at binding energies of 459.1 eV and 464.2 eV correspond to Ti$^{4+}$ [25]. The high resolution spectrum of O1 s includes three peaks (Fig. 8c): the binding energy at 530.3 eV represents the crystal lattice oxygen (Ti$^{4+}$−O/W$^{6+}$−O), indicating that W−O and Ti−O share the orbital O1 s in W−O−Ti linkages. The peak at 531.4 eV corresponds to the surface hydroxyl groups bonded to Ti or W, and the binding energy at 532.8 eV belongs to adsorbed water (H$_2$O$_{ads}$) or

oxygen bonded to carbon (C−O).

The XPS spectrum of W4f core level (Fig. 8d) contains a double peak which can be deconvoluted into two symmetrical peaks at 36.4 eV and 38.4 eV, corresponding to W4f$_{7/2}$ and W4f$_{5/2}$ bonds respectively. These doublet energy bonds represent the W$^{6+}$ oxidation states. The corresponding W4f$_{7/2}$ and W4f$_{5/2}$ spin-orbital separation is 2.1 eV [38], which agrees with the theoretical value for WO$_3$.

In conclusion, XPS data clearly demonstrate that the photocatalyst surface contain Ti and W in the oxidation state of Ti$^{4+}$ and W$^{6+}$ and no other oxidation states were detected. We further verify this by calculating the O/T and O/W ratio from their relative peaks areas and atomic sensitivity factor ($S$).

$$\text{Atomic Ratio} \frac{O}{Ti} = \frac{\frac{I_0}{S_O}}{\frac{I_{Ti}}{S_{Ti}}} = \frac{\frac{174041.63}{0.66}}{\frac{225662.04}{1.8}} = 2.10;$$
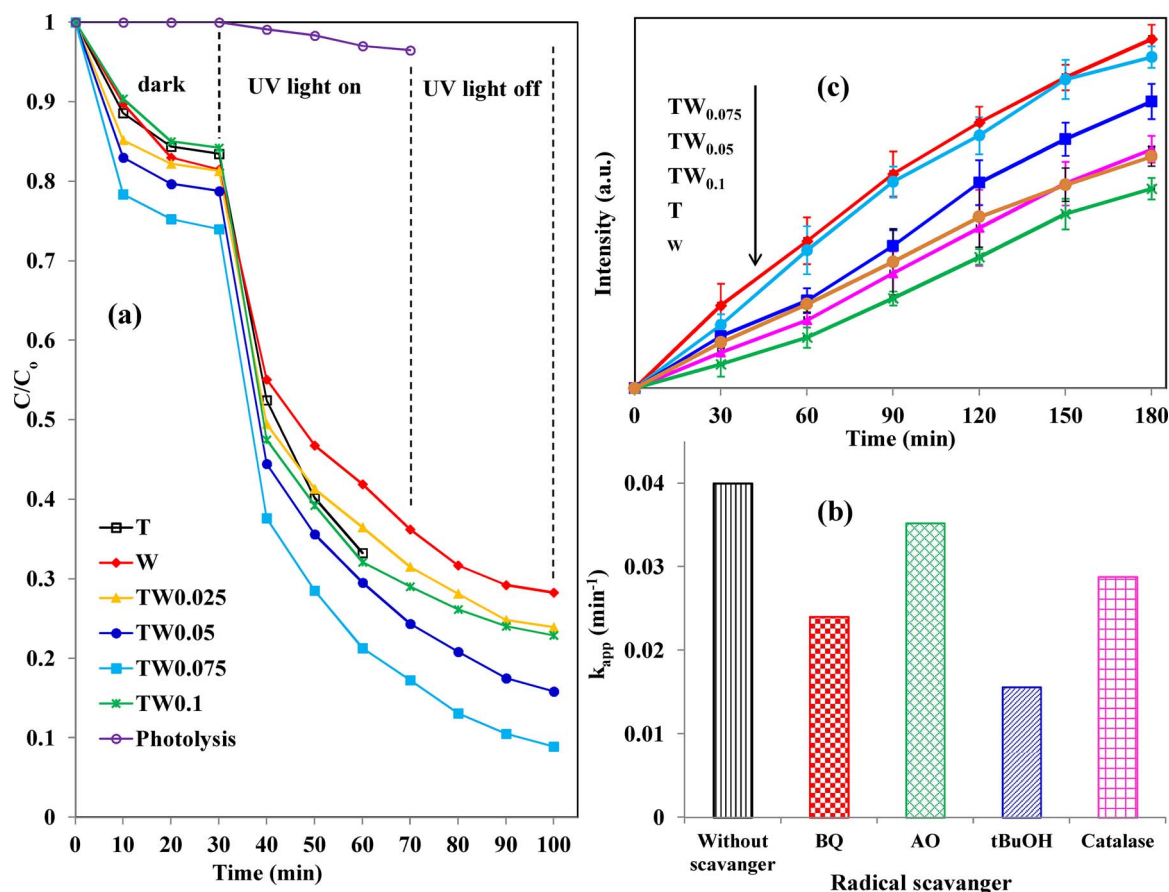
**Fig. 9.** (a) Methylene blue adsorption and degradation in the presence and absence of UV light, (b) change in PL intensity of the dispersed TA solution under UV illumination with the calcined photocatalysts and (c) apparent first-order constant ($k_{app}$) for the degradation of MB solution by $TW_{0.075}$ with and without different scavengers.

$$\text{Atomic Ratio} \frac{O}{W} = \frac{\frac{I_O}{S_O}}{\frac{I_W}{S_W}} = \frac{\frac{286121.89}{0.66}}{\frac{398769.02}{2.75}} = 2.99$$

### 3.10. Photocatalytic activity

The degradation of methylene blue (MB) in water was the model reaction to test the photocatalytic activity of the samples. MB is chemically stable: there is no significant change neither in the adsorption (dark experiment) or degradation of MB under UV light irradiation (photolysis, 40 min) without a photocatalyst (Fig. 9a). The adsorption equilibrium of the MB adsorption on the catalyst in dark occurred after 30 min. The $TW_{0.075}$ hybrid powder exhibited both higher MB dark adsorption and photocatalytic activity compared to the other samples. It degrades more than 90% MB, while W degrades 70% MB in 100 min (30 min dark + 40 min light + 30 min dark). The UV photodegradation activity followed the order: $TW_{0.075} > TW_{0.05} > TW_{0.1} \approx T > TW0._{025} > W$. The calculated corresponding first order apparent rate constant ($k_{app}$) are 0.04, 0.032, 0.03, 0.03, 0.025, 0.022 min$^{-1}$, respectively. The higher photocatalytic activity in the degradation of MB by $TW_{0.075}$ correlates with its higher BET surface area and pore size, which makes the pores more accessible, with its lower band gap, higher concentration of surface hydroxyl groups (FTIR and XPS) and active anatase [001] planes on the surface (Raman spectroscopy), higher separation of charge carriers and their extended lifetime due to homogenous mixing of the two semiconductors. Photocatalysis is mainly a surface phenomenon: higher surface area translates into a greater reactant adsorption. A lower band-gap generates larger amounts of excitons pair, which ultimately produces the desired radicals ($O_2^-\cdot$ and OH·). A reduced recombination rate is also beneficial for the photocatalytic activity. Surface hydroxyl groups detected by FTIR spectroscopy are beneficial for photocatalytic activity because they scavenge the photogenerated holes that can thus yield hydroxyl radicals (OH·), which unselectively react with pollutant molecules [23]. The anatase [001] is the planes with the greatest pollutant adsorption properties and highest OH· radicals production potential [43]. This also provides a large contact interface [44] for efficient charge separation.

Composites homogeneity is also a key parameter to for the photocatalytic activity. SEM-EDX analysis highlighted how hybrid samples are uniform and densely packed, i.e. mesoporous $TiO_2$ and $WO_3$ are in good contact thus assuring efficient charge separation [45]. Furthermore, as the number of contact points increases the photocatalytic activity increases along. PL analysis confirmed the efficient change separation in the hybrid samples: $TW_{0.075}$ powder has a lower recombination rate compared to control samples T and W, the synergistic effect arising from $TiO_2$ and $WO_3$ substances for effective separation of photoinduced charge carriers (e$^-$ and h$^+$) [46]. In contrast, higher recombination of electron-holes pairs in control samples, besides a lower surface area and short lifetime of the charge carries results in a lower activity (Fig. 9a).

Hybrid samples also store the photogenerated electrons that can then be exploited in the degradation process in the absence of light: $TW_{0.075}$ degrades an extra 10% MB after the light goes off (Fig. 8a). Control T has no energy storage capability, while control W sample degrades an extra 5% MB in the dark. By comparison the hybrid samples showed much more energy storage capacity, in the order: $TW_{0.075} > TW_{0.05} > TW_{0.1} \approx TW_{0.025} > W$. We explain this trend by proposing a mechanism in the following sections.

### 3.11. Role of radical scavenge

The reactions between oxygen with photogenerated electrons ($e^- + O_{2ads} \rightarrow O_2^-$), and between adsorbed water and photogenerated holes ($h^+ + H_2O_{ads} \rightarrow H^+ + OH^{\bullet}_{ads}$) produce reactive oxidizing species (ROS) such as super oxide anions ($O_2^- \cdot$), hydrogen peroxide ($H_2O_2$) and hydroxyl radicals ($OH \cdot$). ROS are responsible for the degradation of aqueous organic compounds besides the direct decomposition of organic compounds with photogenerated holes ($h^+ + organics \rightarrow CO_2 + H_2O$). To probe the mechanism responsible for the UV induced photocatalysis, we conducted tests in the presence of several sacrificial agents including 1,4 benzoquinone (BQ, $5 \, mmol \, L^{-1}$), catalase ($22 \, mg \, L^{-1}$), ammonium oxalate (AO, $0.1 \, g \, L^{-1}$) and *tert*-butanol (*t*BuOH, 2 mL).

To elucidate the formation of $O_2^- \cdot$ species, the scavenger 1,4 benzoquinone is added to the solution ($BQ + O_2^- \cdot \rightarrow BQ^{-\cdot} + O_2$). 1,4 benzoquinone is a superoxide radical quencher via fast electron transfer [47]. This reduced the MB degradation by 40% in the presence of $TW_{0.075}$ photocatalyst under our experimental conditions (Fig. 9b). To probe the formation of $H_2O_2$ in the oxidation process, the enzyme catalase is added to the solution, which catalyzes the dismutation of $H_2O_2$ into $H_2O$ and $O_2$ $\left( 2H_2O_2 \xrightarrow{catalase} 2H_2O + O_2 \right)$. As a result, the photodegrading rate decreased by 28%, illustrating that $H_2O_2$ is essential to removal the pollutant, probably acting as an intermediate and being a source of hydroxyl radicals. *Tert*-butanol and ammonium oxalate scavenge hydroxyl radicals and holes [48]: the degradation rate decreased by 61% and 12%, respectively (Fig. 9b). In conclusion, primary hydroxyl radicals, superoxide anions species followed by hydrogen peroxide and holes ($h^+$) degrade the MB pollutant. To further support the dominant role played by $OH \cdot$ radicals in the photocatalytic process, we monitored the formation of $OH \cdot$ on the surface of the UV illuminated photocatalysts by terephthalic acid (TA) fluorescence as a probe [23,48]. TA promptly reacts with hydroxyl radicals to produce the highly fluorescent 2-hydroxy terephathalic acid ($TA + OH^{\bullet} \rightarrow TAOH$). We report the TAOH fluorescence intensity as a function of UV illumination time (Fig. 9). $TW_{0.075}$ and $TW_{0.05}$ produce a larger amount of hydroxyl radicals compared to the rest of the samples, which agrees with the photocatalytic activity data in Fig. 9a. Coupling the two semiconductors improves the light absorption thus generating more charge carriers to produce the hydroxyl radicals, which are the active species in the MB degradation.

### 3.12. Proposed mechanism

We propose a mechanism for the transfer pathways of the photogenerated charge carriers in the hybrid powders ($TW_x$) that are highly active in the degradation of the methylene blue (MB) (Fig. 10). UV light irradiation excites electrons from the valance band (VB) to the conduction band (CB) of $TiO_2$ and $WO_3$ semiconductors (SC), while leaving holes in the VB ($SC_{TiO_2/WO_3} + h\vartheta \rightarrow e_{CB}^- + h_{VB}^+$). The oxygen supplied from the bulk readily reacts with the excited electrons in $TiO_2$ CB band to produce the highly reactive superoxide anions and other oxygen reactive species ($O_2 + e^- \rightarrow O_2^- \cdot (aq)$, $-0.33 V \, vs \, NHE$); ($O_2 + e^- \rightarrow O_2^- (aq)$, $-0.284 V \, vs \, NHE$); ($O_2 + H^+ + e^- \rightarrow HO_2 (aq)$, $-0.046 \, vs \, NHE$) [49,50]. This happens because the CB energy level of $TiO_2$ is more negative (Table 3) than the potential for the single electron reduction of oxygen. In comparison, the CB level of $WO_3$ is more positive (Table 3) than the reduction potential of $O_2$, thus $WO_3$ (control W) alone is inefficient to decompose organic compounds (Fig. 9a). The VB holes ($h^+$) produce hydroxyl radicals ($h^+ + H_2O \rightarrow OH^{\bullet} + H^+$; $h^+ + OH^- \rightarrow OH^{\bullet}$). Superoxide anions ($O_2 \cdot^-$) and hydroxyl radicals ($OH \cdot$), besides photogenerated VB holes ($h^+$) oxidize MB molecules.

$TiO_2$ CB potential is more negative than that of $WO_3$, and the
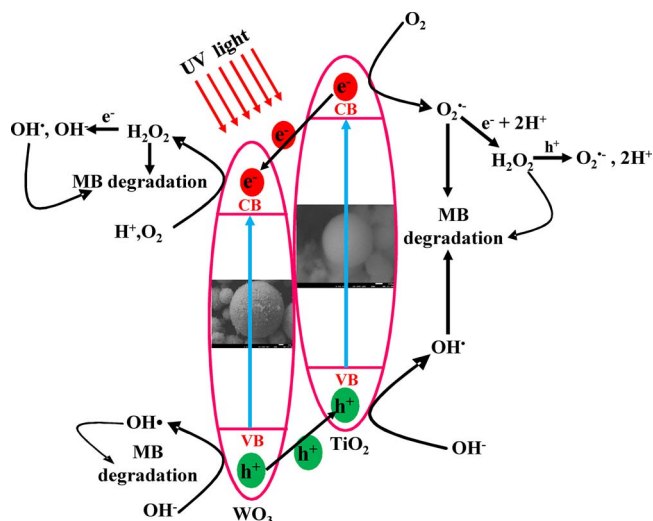


**Fig. 10.** Proposed mechanism illustrating the transfer pathways of the produced charge carriers and various oxidizing species contributing to the degradation of MB.

potential of $WO_3$ VB is more positive than that of $TiO_2$ (Table 3). This means that upon light irradiation there is a greater possibility that the excited electrons from $TiO_2$ CB transfer to $WO_3$ CB rather than the opposite, whereas holes would be preferably injected from the VB of $WO_3$ to the VB of $TiO_2$. This further depicts how $TiO_2$ acts as an electron generator and $WO_3$ plays the role of electron receiver with light irradiation, regenerating the catalyst. Such a transfer of exciton pairs results in greater charge separation reduced recombination phenomena and increased lifetime of charge carriers (PL and TRPL analysis). In the absence of light irradiation, the stored electrons in $WO_3$ CB band produce oxidizing species such as hydrogen peroxide ($O_2 + 2H^+ + 2e^- \rightarrow H_2O_2 (aq)$, $+0.682 V \, NHE$), which generates hydroxyl radicals upon further reduction ($H_2O_2 + e^- \rightarrow OH^- + OH^{\bullet} (aq)$) [51]. The produced hydroxyl ions scavenge the holes in VB and yield $OH \cdot$ radicals, which further decompose the pollutant. $H_2O_2$ also react with valance band holes ($h^+$) to produce superoxide anion ($h^+ + H_2O_2 \rightarrow O_2^- \cdot + 2H^+$) thus acting as a hole scavenger and preventing recombination [52].

In summary, $WO_3$ confers energy storage properties to the hybrid $TiO_2/WO_3$ samples, increasing their photocatalytic activity. The electrons stored in the $WO_3$ CB band readily react to powerful oxidizing agents such as $H_2O_2$, $OH \cdot$ in the absence of light irradiation.

## 4. Conclusions

We synthesized control (T, W) and hybrid $TiO_2/WO_3$ samples ($TW_x$; x is 0.025, 0.5, 0.075, 0.1 molar ratio of W precursor) via facile sol–gel and crash precipitation methods followed by drying. This method homogeneously dispersed and intimately mixed the nanometric oxide crystallites (20 nm) in a high-surface porous powder ($200 \, m^2/g$). In the photocatalytic degradation of methylene blue (MB) in liquid phase hybrid samples were the most active: $TW_{0.075}$ degraded 90% MB in 100 min (30 min dark + 40 min light + 30 min dark), while W was least active with 70% MB degradation. $TW_{0.075}$ was also the most active sample in the dark, degrading an extra 10% MB after the light went off. $TiO_2$ and $WO_3$ act in synergy: because of the difference in band potential of the semiconductors, electrons diffuse from the conduction band of $TiO_2$ to that of $WO_3$ upon UV light irradiation. Consequently, the lifetime of electron-hole pairs increases and the recombination rate decreases, thus enhancing the photocatalytic activity. Tests with several scavengers highlighted how the active species $OH \cdot$ (hydroxyl radicals) followed by $O_2 \cdot^-$ (super oxide anions), play a major role in the degradation of MB. Photoluminescence after reaction with terephthalic acid method confirmed that hybrid samples produce more hydroxyl

radicals. Besides the greater charge separation, the higher BET surface area of $TW_{0.075}$, $TW_{0.5}$ result in a higher concentration of hydroxyl ions on the surface, which act as holes trap that can then react to produce further OH· radicals. The FTIR and XPS data support this result, which confirms the presence of hydroxyl ions on the catalyst surface.

The results from this work suggest new avenues to design, develop and apply $TiO_2$ coupled semiconductor photocatalysts with enhanced photocatalytic activity and greater electron storage ability.

## Conflicts of interest

The authors declare that there is no conflict of interests regarding the publication of this paper.

## Acknowledgments

## Appendix A. Supplementary data

Supplementary data associated with this article can be found, in the online version, at https://doi.org/10.1016/j.apcatb.2017.12.049.

## References

[1] W.J. Zhou, Y.H. Leng, D.M. Hou, H.D. Li, L.G. Li, G.Q. Li, H. Liu, S.W. Chen, Nanoscale 6 (2014) 4698–4704.
[2] C. Pirola, D.C. Boffito, S. Vitali, C.L. Bianchi, J. Coat. Technol. Res. 9 (2012) 453–458.
[3] H. Khan, D. Berk, J. Photochem. Photobiol. A: Chem. 294 (2014) 96–109.
[4] Y.F. Li, D. Xu, J. Oh, W. Shen, X. Li, Y. Yu, ACS Catal. 2 (2012) 391–398.
[5] M. Stucchi, C.L. Bianchi, C. Argirusis, V. Pifferi, B. Neppolian, G. Cerrato, D.C. Boffito, Ultrason. Sonochem. 40 (2018) 282–288.
[6] M. Ni, M.K.H. Leung, D.Y.C. Leung, K. Sumathy, Renew. Sustain. Energy Rev. 11 (2007) 401–425.
[7] S.G. Kumar, L.G. Devi, J. Phys. Chem. A 115 (2011) 13211–13241.
[8] D.C. Boffito, V. Crocella, C. Pirola, B. Neppolian, G. Cerrato, M. Ashokkumar, C.L. Bianchi, J. Catal. 297 (2013) 17–26.
[9] J. Yan, G. Wu, N. Guan, L. Li, J. Appl. Catal. B: Environ. 152 (2014) 280–288.
[10] X.Z. Li, F.B. Li, C.L. Yang, W.K. Ge, J. Photochem. Photobiol. A: Chem. 141 (2001) 209–217.
[11] D. Guerrero-Araque, D. Ramírez-Ortega, P. Acevedo-Pena, F. Tzompantzi, H.A. Calderon, R. Gomez, J. Photochem. Photobiol. A: Chem. 335 (2017) 276–286.
[12] S. Supothina, P. Seeharaj, S. Yoriya, M. Sriyudthsak, Ceram. Int. 33 (2007) 931–936.
[13] D. Su, J. Wang, Y. Tang, C. Liu, L. Liu, X. Han, Chem. Commun. 47 (2011) 4231–4233.
[14] S. Eibl, B.C. Gates, H. Knozinger, Langmuir 17 (2001) 107–115.
[15] N. Saadatkhah, M.G. Rigamonti, D.C. Boffito, H. Li, S.G. Patience, Powder Technol. 316 (2017) 434–440.
[16] H. Yang, R. Shi, K. Zhang, Y. Hu, A. Tang, X. Li, J. Alloys Compd. 398 (2005) 200–202.
[17] D. Ke, H. Liu, T. Peng, X. Liu, K. Dai, Mater. Lett. 62 (2008) 447–450.
[18] Y.R. Do, W. Lee, K. Dwight, A. Wold, J. Solid State Chem. 108 (1994) 198–201.
[19] S.A.K. Leghari, S. Sajjad, F. Chen, J. Zhang, Chem. Eng. J. 166 (2011) 906–915.
[20] G. Zerjav, M.S. Arshad, P. Djinovic, J. Zavasnik, A. Pintar, Appl. Catal. B: Environ. 209 (2017) 273–284.
[21] K.K. Akurati, A. Vital, J.P. Dellemann, K. Michalow, T. Graule, D. Ferri, A. Baiker, Appl. Catal. B: Environ. 79 (2008) 53–62.
[22] L.J. Alemany, M.A. Larrubia, M.C. Jiménez, F. Delgado, J.M. Blasco, React. Kinet. Catal. Lett. 60 (1997) 41–47.
[23] H. Khan, React. Kinet. Mech. Catal. (2017) 1–22.
[24] M. Thommes, K. Kaneko, A.V. Neimark, J.P. Olivier, F.R. Reinoso, J. Rouquerol, K.S.W. Sing, Pure Appl. Chem (2015) 1–19.
[25] H. Khan, D. Berk, Appl. Catal. A: Gen. 505 (2015) 285–301.
[26] R.Q. Cabrera, E.R. Latimer, A. Kafizas, C.S. Blackman, C.J. Carmalt, I.P. Parkin, J. Photochem. Photobiol. A 239 (2012) 60–64.
[27] J.R.G. Navarro, A. Mayence, J. Andrade, F. Lerouge, F. Chaput, P. Oleynikov, L. Bergström, S. Parola, A. Pawlicka, Langmuir 30 (2014) 10487–10492.
[28] P. Chen, M. Qin, D. Zhang, Z. Chen, B. Jia, Q. Wan, H. Wu, X. Qu, Cryst. Eng. Comm. 17 (2015) 5889–5894.
[29] B. Xiao, Q. Zhao, C. Xiao, T. Yang, P. Wang, F. Wang, X. Chen, M. Zhang, Cryst. Eng. Comm. 17 (2015) 5710–5716.
[30] N. Siedl, S.O. Baumann, M.J. Elser, O. Diwald, J. Phys. Chem. C 116 (2012) 22967–22973.
[31] M. Miskam, K. N, A. Bakar, S. Mohamad, J. Sol–Gel Sci. Technol. 67 (2013) 121–129.
[32] H. Khan, D. Berk, Catal. Lett. 144 (2014) 890–904.
[33] C. Guery, C. Choquet, F. Dujeancourt, J.M. Tarascon, J.C. Lassegues, J. Solid State Electrochem. 1 (1997) 199–207.
[34] K. Jothivenkatachalam, S. Prabhu, A. Nithya, K. Jeganathan, RSC Adv. 4 (2014) 21221–21229.
[35] J.D. Reyes, V.D. Garcia, A.P. Benitez, J.A.B. Lopez, Superficies y Vacio 21 (2008) 12–17.
[36] X. Zheng, Q. Yang, S. Huang, J. Zhong, J. Li, R. Yang, Y. Zhang, J. Sol–Gel Sci. Technol. 83 (2017) 174–180.
[37] J. Theerthagiri, R.A. Senthil, A. Malathi, A. Selvi, J. Madhavan, M. Ashokkumar, RSC Adv. 5 (2015) 52718–52725.
[38] S.K. Chong, C.F. Dee, S.A. Rahman, RSC Adv. 5 (2015) 2346–2353.
[39] S. Adhikari, D. Sarkar, H.S. Maiti, Mater. Res. Bull. 49 (2014) 325–330.
[40] F. Tian, Y. Zhang, J. Zhang, C. Pan, J. Phys. Chem. C 116 (2012) 7515–7519.
[41] B. Choudhury, A. Choudhury, Physica E: Low Dimens. Syst. Nanostruct. 56 (2014) 364–371.
[42] B. Choudhury, A. Choudhury, J. Lumin. 136 (2013) 339–346.
[43] Y.J. Yuan, Z.J. Ye, H.W. Lu, B. Hu, Y.H. Li, D.H. Chen, J.S. Zhong, Z.T. Yu, Z.G. Zou, ACS Catal. 6 (2016) 532–541.
[44] Y. Nosaka, M. Nishikawa, Y.A. Nosaka, Molecules 19 (2014) 18248–18267.
[45] N. Lakshminarasimhan, E. Bae, W. Choi, J. Phys. Chem. C 111 (2007) 15244–15250.
[46] L. Chen, S. Yang, B. Hao, J. Ruan, P.C. Ma, Appl. Catal. B: Environ. 166–167 (2015) 287–294.
[47] J. Bandara, J. Kiwi, New J. Chem. 23 (1999) 717–724.
[48] N. Zhang, S. Liu, X. Fu, Y.J. Xu, J. Phys. Chem. C 115 (2011) 9136–9145.
[49] J. Li, Y. Liu, Z. Zhu, G. Zhang, T. Zou, Z. Zou, S. Zhang, D. Zeng, C. Xie, Sci. Rep. 3 (2013) 1–6.
[50] M. Lu, P. Pichat, ACS Energy Lett. 1 (2016) 356–359.
[51] Y. Nosaka, A. Nosaka, ACS Energy Lett. 1 (2016) 356–359.
[52] Y. Kakuma, A.Y. Nosaka, Y. Nosaka, Phys. Chem. Chem. Phys. 17 (2015) 18691–18698.